

GWBENCH: a novel Fisher information package for gravitational-wave benchmarking

S. Borhanian^{1,2}

¹*Institute for Gravitation and the Cosmos, Department of Physics, Pennsylvania State University, University Park, PA 16802, USA*

²*Theoretisch-Physikalisches Institut, Friedrich-Schiller-Universität Jena, 07743, Jena, Germany**

(Dated: February 1, 2022)

We present a new PYTHON package, **GWBENCH**, implementing the well-established Fisher information formalism as a fast and straightforward tool for the purpose of gravitational-wave benchmarking, i.e. the estimation of signal-to-noise ratios and measurement errors of gravitational waves observed by a network of detectors. Such an infrastructure is necessary due to the high computational cost of Bayesian parameter estimation methods which renders them less effective for the scientific assessment of gravitational waveforms, detectors, and networks of detectors, especially when determining their effects on large populations of gravitational-wave sources spread throughout the universe. **GWBENCH** further gives quick access to detector locations and sensitivities, while including the effects of Earth's rotation on the latter, as well as waveform models and their derivatives, while giving access to the host of waveforms available in the LSC Algorithm Library. With the provided functionality, **GWBENCH** is relevant for a wide variety of applications in gravitational-wave astronomy such as waveform modeling, detector development, cosmology, and tests of general relativity.

I. INTRODUCTION AND MOTIVATION

The initial detections of gravitational waves (GWs) emitted during the coalescences of black holes and neutron stars [1, 2] have confirmed a fundamental prediction of general relativity and opened a new observational window into the universe in the same breath. Further detections by the LIGO and Virgo observatories have pushed the number of observed GW signals into the decades [3], and hence set off the era of GW astronomy. This success has ignited the desire for detections that allow for better estimation of the information buried in the signals that the GW observatories record, thus allowing us to reveal new phenomena and novel physics as well as shed light into greater depths of the cosmos.

Such desires pose challenges on many essential components in the figurative GW detection machinery, with the development of new waveform (WF) models and the planning of future detector designs being two important tasks to tackle. The former is imperative to lower the systematic biases in what kind of signals the observatories will be able to detect, to increase the information that can be extracted from the detector output, and possibly to lower the computational cost of WF model evaluation. The inclusion of higher-order spherical harmonic modes beyond the quadrupole [4, 5] is one such example illustrating the impact of improved WF models as it enhances the detectability of binaries whose orbits are highly inclined with respect to the line of sight and allows for an improved parameter estimation by lifting the degeneracy between luminosity distance and inclination angle.

The detector challenge is even more fundamental: new, ground-breaking analyses require ‘richer’ data to forge through. The current, so called second-generation (2G) of GW detectors, LIGO Hanford and Livingston [6] as well as Virgo [7], will be joined by two more detectors, KAGRA [8] and LIGO-India [9], and further sensitivity improvements are planned to go in effect in the years to follow [10, 11]. Nevertheless the limits

of these facilities to address future, scientific goals are already apparent [12, 13]. Thus the GW community has been pursuing the conceptualization of the next generation of detectors. The proposals range from the Voyager effort, envisioning a multitude of upgrades to the LIGO facilities [14], to completely new, third-generation (3G) observatories, namely the Einstein Telescope [13, 15, 16] and the Cosmic Explorer effort [17]. In addition, efforts are under way to search for GW from space, with the Laser Interferometer Space Antenna (LISA) [12].

Independently of what WF models shall be developed and adopted, or which facilities continue or start operating, the GW community will need tools to *benchmark* the scientific output of any combination of these two components in a quick and efficient way. One such tool is the Fisher information formalism (FIF) [18, 19] which has proven to be a viable method for GW benchmarking. Its major caveat is its dependence on high signal-to-noise ratios to give reliable results, thus making it mostly suitable to exceptional events in current detectors. Nevertheless, the formalism is very useful and widely applicable in studies entailing future generations of detectors. For an extended review on the caveats of the FIF we refer to [20]. Further, developments to improve the speed of full Bayesian parameter estimation, for example via the application of machine learning techniques [21–24], could make the Bayesian framework a viable benchmarking tool in the future.

In this work, we present a new PYTHON package, **GWBENCH**, that implements the FIF in an easy-to-use manner and further provides means to compute and access a host of quantities that are necessary for benchmarking. For a selection of GW detectors, a so-called *network*, and given a WF model, **GWBENCH** can compute: plus and cross polarizations of the WF, detector power spectral densities, antenna patterns, location phase factors, detector responses, detector and network signal to noise ratios, and measurement errors in the WF model parameters from the FIF. Two particularly substantial features are the inclusion of WFs from the LSC Algorithm Library (LAL) [25, 26] and the capability to include the effects of Earth's rotation in the detector antenna patterns.

The paper is structured as follows: Section II introduces the Cosmic Explorer trade study which stimulated the develop-

* ssohrab.borhanian@uni-jena.de

ment of this package. In Section III we briefly review the FIF and aforementioned core concepts utilized by **GWBENCH**. Next, we show a straightforward example application of **GWBENCH** to showcase its functionality in Section IV and proceed to present a few validation tests of the core methods of **GWBENCH** in Section V. In Section VI, we describe the application of the code in two previous papers and conclude this work in Section VII.

II. COSMIC EXPLORER TRADE STUDY

The Cosmic Explorer Project¹ aims to develop among other things the science case for a next-generation GW detector, the Cosmic Explorer (CE). CE is a promising US proposal for a ground-based detector design which is targeting to answer a wide variety of scientific questions [27–31] as part of a global network of GW observatories. These questions are grouped under three overarching *science goals*: (i) dynamics of dense matter and extreme environments, (ii) black holes and neutron stars through cosmic time, and (iii) extreme gravity and fundamental physics. The questions encompass a broad range of fields relevant to GW astronomy including but not restricted to neutron star physics, cosmology, tests of general relativity, and the feasibility of multi-messenger observations.

GWBENCH was developed to perform an exhaustive *trade study* to gauge CE’s performance in reaching the set science goals. The trade study examines some 457 global GW detector networks combining 50 CE configurations with plausible background detectors such as upgraded 2G facilities or the Einstein Telescope. Besides the number of networks, the computational requirements are also driven by the list of science questions to be answered.

Hence, we decided to implement the FIF in **GWBENCH**, as it allows us to perform the required tasks effectively for many events and different waveform models in each network of interest. The measurement error estimates computed from the FIF are processed to obtain pre-defined performance metrics which in return allow us to evaluate the science potential of the various network configurations. Such metrics are for example the signal-to-noise ratios, 90%-credible sky areas, expected event rates, and measurement error estimates on WF parameters, but also on inferred quantities such as neutron star radii.

As such, **GWBENCH** has an important role to play for the development of CE’s science case. The broad range of science goals that can be examined with the code showcases that **GWBENCH** is a powerful tool that has a wide variety of applications in gravitational-wave astronomy. We present two of our recent studies that were enabled by **GWBENCH** in Section VI.

III. CONCEPTS FOR GRAVITATIONAL WAVE BENCHMARKING

GWBENCH implements a variety of standard concepts and aims to make them easily accessible to the user. We briefly review

them [32] in this section.

Waveform polarizations: Gravitational waves are emitted by a host of astrophysical and cosmological phenomena, with the coalescence of compact binaries as the most prominent example. The incoming GWs can be decomposed into two polarizations, *plus* $h_+(t; \Theta_{GW})$ and *cross* $h_\times(t; \Theta_{GW})$, and carry an abundance of information about their source systems, encoded in the parameter vector Θ_{GW} . This vector depends on the WF model. In case of the coalescence of two black holes the standard set of such parameters, $\Theta_{GW} = \{m_1, m_2, \chi_1, \chi_2, D_L, \iota, t_c, \phi_c\}$ contains the companion masses m_1, m_2 and dimensionless spin vectors χ_1, χ_2 , the binary’s luminosity distance D_L , the inclination angle ι of its orbital plane with respect to the line of sight, as well as two integration parameters: the time t_c and phase ϕ_c of coalescence.

In the remainder of this manuscript, we will use the Fourier transforms of the WF and other quantities in the frequency-domain:

$$H_{+/\times}(f) = \int_{-\infty}^{\infty} dt h_{+/\times}(t) e^{i2\pi ft}. \quad (3.1)$$

Antenna patterns and location phase factor: The quadrupolar nature of GWs results in sky-position dependent responses from detectors to incoming waves. The responses are governed by the so-called *antenna pattern functions* F_+ and F_\times which are functions of the source’s sky position—right ascension α and declination δ —and polarization angle ψ . Besides, the relative motion between the source and detector results in a frequency-dependence in the Fourier-domain [33, 34]; albeit being negligible for signals that are short compared to the time scale of the motion.

Another group of important quantities that encode the spatial distribution of detectors in networks are the *location phase factors* F_{lp} which shift the phase of the detector responses appropriately for each detector:

$$F_{lp} = \exp[i2\pi f/c \hat{\mathbf{r}}(\alpha, \delta) \cdot \mathbf{d}(\alpha_d, \beta_d)], \quad (3.2)$$

where $\hat{\mathbf{r}}$ and \mathbf{d} are the unit vector pointing to the source and the position vector of the detector, respectively, if measured from the center of Earth. α_d and β_d are the detector’s longitude and latitude, respectively.

Detector response: The aforementioned *detector response* H is the GW strain in the frequency-domain measured by a detector, combining the WF polarizations with the detector’s antenna patterns and location phase factor. It differs from the actually recorded detector output $s(t) = h(t) + n(t)$ in the time-domain or $S(f) = H(f) + N(f)$ in the frequency-domain, which also contains contributions from the detector noise $n(t)$ or $N(f)$, respectively. The detector response is given by

$$H(f; \Theta) = F_{lp}(f; \alpha, \delta) \cdot [H_+(f; \Theta_{GW}) F_+(f; \alpha, \delta, \psi) + H_\times(f; \Theta_{GW}) F_\times(f; \alpha, \delta, \psi)], \quad (3.3)$$

where $\Theta = \{\Theta_{GW}, \alpha, \delta, \psi\}$.

¹ <https://cosmicexplorer.org/>

Power spectral density: The sensitivity of a detector determines its ability to measure the strain H . It is governed by systematics due to detector noise $n(t)$ and characterized by the noise auto-correlation $\kappa = \overline{n(t_1)n(t_2)}$ ². In the following, we assume the noise to be stationary and Gaussian, with mean $\bar{n} = 0$. The former assumption ensures that κ only depends on the time-difference $t^* = t_1 - t_2$. Thus, the *one-sided power spectral density* (PSD) S_n —the Fourier transform of κ for positive frequencies and thus its frequency-domain counterpart—is given by

$$S_n(f) = \frac{1}{2} \int_{-\infty}^{\infty} dt^* \kappa(t^*) e^{i2\pi f t^*}, \text{ with } f > 0. \quad (3.4)$$

$S_n(f)$ indicates the sensitivity of the detector at different GW frequencies.

Noise-weighted scalar product and signal-to-noise ratio: The existence of noise in the detector output affects the detection and measurement of the GW signal strain, obscuring the difference between various detector responses to some level. One way to assess the *overlap* of these responses in a manner that takes the detector's sensitivity into account is by defining a *noise-weighted scalar product* [32],

$$\langle H, G \rangle = 2 \int_0^{\infty} df \frac{H(f)G^*(f) + H^*(f)G(f)}{S_n(f)}, \quad (3.5)$$

where H, G are two detector responses, e.g. for two different WF models or the same model evaluated at different parameters.

Given this scalar product, we can calculate the *signal-to-noise ratio* (SNR) ρ of a given detector response H for a given detector PSD S_n as

$$\rho^2 = \langle H, H \rangle = 4 \int_0^{\infty} df \frac{|H(f)|^2}{S_n(f)}, \quad (3.6)$$

indicating the relative loudness of the detector response compared to the noise in the detector output [32].

Fisher information formalism: The *FIF* or *Fisher analysis* is well-established in GW data analysis and discussed in detail in [18, 19]. Here, we give a brief summary of how it allows us to estimate parameter error bounds.

Since we assumed that the noise $n = s - h$ behaves Gaussian with zero mean, the same holds for its Fourier transform $N = S - H$. Thus, the probability of the noise can be written as

$$p(\Theta) = p^0(\Theta) e^{-\frac{1}{2} \langle S-H(\Theta), S-H(\Theta) \rangle}, \quad (3.7)$$

where Θ and p^0 are the parameter vector of the detector response H and the prior on these parameters, respectively. Then the value of Θ at peak probability is a good estimate of the true value Θ^* for the given GW signal S , assuming a large SNR.

The probability is the greatest when the exponential is the largest³. Around the maximal value, the exponent $E = \langle S - H, S - H \rangle$ can be expanded as

$$E(\Theta) = E(\Theta^*) + \frac{1}{2} \left. \frac{\partial^2 E(\Theta)}{\partial \Theta_i \partial \Theta_j} \right|_{\Theta=\Theta^*} \Delta \Theta_i \Delta \Theta_j + \dots, \quad (3.8)$$

where $\Delta \Theta_i = \Theta_i - \Theta_i^*$. The Hessian

$$\frac{\partial^2 E(\Theta)}{\partial \Theta_i \partial \Theta_j} = 2 \langle \partial_{\Theta_i} H(\Theta), \partial_{\Theta_j} H(\Theta) \rangle + \langle \partial_{\Theta_i} \partial_{\Theta_j} H(\Theta), N \rangle \quad (3.9)$$

reduces for noise with zero-mean to the first summand in which we identify the *Fisher information matrix* (FIM) Γ

$$\Gamma_{ij} \equiv \langle \partial_{\Theta_i} H(\Theta), \partial_{\Theta_j} H(\Theta) \rangle. \quad (3.10)$$

Equations (3.8) and (3.10) inserted in the probability (3.7) yield

$$p(\Theta) \sim e^{-\frac{1}{2} \Gamma_{ij} \Delta \Theta_i \Delta \Theta_j}. \quad (3.11)$$

Thus the assumption of Gaussianity motivates the association of the FIM to be the inverse of the *covariance matrix* $\Sigma \equiv \Gamma^{-1}$. The diagonal and off-diagonal elements of Σ denote the variances and covariances of the parameters, respectively, due to the uncertainty introduced by the detector noise and give 1σ -error estimates via $\sigma_{\Theta_i} = \sqrt{\Sigma_{ii}}$.

Detector networks and associated quantities: The above definitions of the SNR ρ and FIM Γ depend on quantities such as the detector response and PSD and are therefore inherently detector-specific. In a network, detectors work in tandem to improve detectability and parameter estimation which can be captured by defining *network versions* of the SNR and FIM

$$\rho_{\text{net}}^2 = \sum_{n=1}^{N_d} \rho_n^2, \quad (3.12)$$

$$\Gamma_{\text{net}} = \sum_{n=1}^{N_d} \Gamma_n, \quad (3.13)$$

where N_d is the number of detectors in the network and ρ_n and Γ_n are the SNR and FIM of the n -th detector, respectively. Consequently, the network covariance matrix and error estimates follow from Γ_{net} as defined before.

Condition number of the Fisher information matrix: If the covariance matrix is obtained via numerical inversion, the FIM needs to be well-conditioned which can be checked with the condition number $c_\Gamma = e_{\max}/e_{\min}$. Here, e_{\max}, e_{\min} are the largest and smallest eigenvalues of Γ . If the condition number exceeds a critical value—a conservative choice for double-precision is $c_{\text{crit}} = 10^{15}$ [35]—the inversion result cannot be trusted generically and should thus be disregarded.

IV. GRAVITATIONAL WAVE BENCHMARKING WITH GWBENCH

A. Package overview

The installation instructions for GWBENCH and the source code are publicly available on GItLAB: <https://gitlab.com>.

² The average is taken with respect to an ensemble of noise realizations. The times t_1 and t_2 are any two arbitrary times at which the detector noise is evaluated or measured.

³ [19] shows that this holds even for non-flat priors p^0 .

[com/sborhanian/gwbench](https://github.com/sborhanian/gwbench). The package consists of 33 modules which implement the concepts discussed in Section III as well as several WFs models. In this section, we will demonstrate with the aid of a few examples how to use the main module of GWBENCH, `NETWORK`, to perform GW benchmarking. These examples are available as PYTHON scripts at https://gitlab.com/sborhanian/gwbench/-/tree/master/example_scripts.

`NETWORK` contains the `Network` class, see Appendix A, which is designed to handle the concepts introduced in Section III—detector initialization (antenna patterns, location phase factors, and PSDs), WF evaluation, and both SNR and error benchmarking—by conducting and facilitating the tasks of the other modules in the package. We will refer to the appendices as needed to discuss these modules and aspects of the package.

B. Basic application using GWBENCH

We begin with a step-by-step showcase of the basic usage of the `Network` module following the example script `QUICK_START.PY`. In this example we estimate the SNR, measurement errors, and 90%-credible sky area for a signal with the same masses as the first detected GW event GW150914 [1], if it was measured by three detectors at the LIGO sites in Hanford, WA and Livingston, LA and the Virgo site in Cascina, Italy. Each detector is set to the aLIGO detector sensitivities [6] and we perform the Fisher analysis with the WF model TaylorF2 [36–43], see Appendix B.

We begin by importing the `NUMPY` and `GWBENCH.NETWORK` modules and specify the `network_spec` which tells the `Network` which `Detector` instances to initialize: `['aLIGO_H', 'aLIGO_L', 'aLIGO_V']` will result in three detectors with aLIGO technology, located and oriented like the Hanford, Livingston, and Virgo detectors (refer to the Appendices C and D for other sites and sensitivities available in GWBENCH).

```
import numpy as np
from gwbench import network
```

```
network_spec = ['aLIGO_H', 'aLIGO_L', 'aLIGO_V']
net = network.Network(network_spec)
```

While the `Network` class is the main interaction point for the user, single-detector tasks are relayed to the `Detector` class. Appendix A compares these two classes to show their similarities and how they synergize to conduct the GW benchmarking together.

Next, we choose the WF model of interest, TaylorF2, and initialize the `Waveform` object inside our `Network`. `Waveform` is another important class that handles WF selection and evaluation. Appendix B contains a brief description of this class and the full list of available WF models in GWBENCH, at the time of writing this paper.

```
wf_model_name = 'tf2'
net.set_wf_vars(wf_model_name=wf_model_name)
```

Finally, we need to set a few `Network` variables like the frequency array and injection parameters in the detector frame, used for WF evaluation. Further, the code needs to know with respect to which of these parameters to take derivatives for the FIM. Besides, we can set the `Network` to convert the derivatives ∂_p and errors σ_p for certain parameters p into the cosine ($\partial_{\cos(p)}$ and $\sigma_{\cos(p)}$) or logarithmic ($\partial_{\log(p)}$ and $\sigma_{\log(p)}$) versions. The final option tells the code whether to take Earth's rotation into account for the computation of the antenna pattern functions, see Appendix C.

```
f = np.arange(5., 61.5, 2**-4)
```

```
inj_params = {
    'Mc': 30.9,
    'eta': 0.247,
    'chilz': 0,
    'chi2z': 0,
    'DL': 475,
    'tc': 0,
    'phic': 0,
    'iota': np.pi/4,
    'ra': np.pi/4,
    'dec': np.pi/4,
    'psi': np.pi/4,
    'gmst0': 0
}
```

```
deriv_syms_string = 'Mc eta DL tc phic iota ra dec psi'
```

```
conv_cos = ('iota', 'dec')
conv_log = ('Mc', 'DL')
```

```
use_rot = 0
```

```
net.set_net_vars(
    f=f, inj_params=inj_params,
    deriv_syms_string=deriv_syms_string,
    conv_cos=conv_cos, conv_log=conv_log,
    use_rot=use_rot
)
```

The high frequency cutoff of 61.5 Hz corresponds to the GW frequency at the innermost stable circular orbit of a compact binary coalescence with total detector-frame mass $M = \mathcal{M}/\eta^{3/5} = 71.5 M_\odot$ for the example injections with detector-frame chirp mass $\mathcal{M} = 30.9 M_\odot$ and symmetric mass ratio $\eta = 0.247$. The detector-frame masses correspond to redshifted sources-frame masses of GW150914, i.e. $m_{\text{det}} = m_{\text{source}}(1+z)$ where we used a fiducial value of $z = 0.1$ and computed the luminosity distance via Planck18 cosmology from the `ASTROPY` package [44, 45]. `gmst0` is the Greenwich Mean Sidereal Time when the signal passes Earth's center.

The `Network` is prepared for benchmarking and we calculate the WF polarizations and their derivatives with respect to the chosen parameters with the following function calls.

```
net.calc_wf_polarizations()
net.calc_wf_polarizations_derivs_num()
```

The first line only computes the plus and cross polarizations in the frequency-domain, `net.hfp` and `net.hfc`, while the second obtains a dictionary `net.del_hfpc` containing the derivatives of the two WF polarizations, in addition to that. The structure of these *derivative dictionaries* is detailed in Appendix E.

Next, we setup antenna patterns, location phase factors, and PSDs for each Detector in the Network .

```
net.setup_ant_pat_lpf_psd()
```

The calculated quantities can be accessed in each Detector instance via `net.detectors[i].fp`, `net.detectors[i].fc`, `net.detectors[i].flp`, and `net.detectors[i].psd` for $i = 0, \dots, N_d - 1$. We note that the Detector automatically truncates the frequency array, if necessary, to the range dictated by the given detector's PSD. This truncation is saved in `net.detectors[i].f` for $i = 0, \dots, N_d - 1$ and translates to all consecutive computations which depend on the frequency, e.g. in the detector response or the location phase factor, and is necessary to avoid array-length mismatches within a Detector instance. On the other hand, it can result in a mismatch when comparing frequency-dependent quantities of two Detector instances or between the Network and one of its Detectors.

With antenna patterns and location phase factors prepared, we can calculate the detector responses and their derivatives, analogously to the case for the WF polarizations.

```
net.calc_det_responses()
net.calc_det_responses_derivs_num()
```

The evaluated responses and derivative dictionaries can be accessed in each Detector instance via `net.detectors[i].hf` and `net.detectors[i].del_hf` for $i = 0, \dots, N_d - 1$.

With the previously computed PSDs, we obtain readily the detector and network SNRs.

```
net.calc_snrs()
```

The function calculates both ρ and ρ^2 for the total network and each detector in the network. The values are saved in the respective Network and Detector instances.

Finally, we compute the error estimates on the parameters specified in `deriv_syms_string` and the estimates of the 90%-credible sky area.

```
net.calc_errors()
net.calc_sky_area_90()
```

```
net.print_detectors()
net.print_network()
```

`calc_errors` contains several steps: It starts by calculating the FIMs for all the Detector instances and then the Network one from those. Next, it computes and saves the condition number c_F for each FIM Γ , and checks if the matrices are well-conditioned ($c_F < 10^{15}$). If this criterion is fulfilled, the code will proceed to invert each FIM to obtain all the covariance

matrices Σ and consequently the error estimates. Finally, it calculates the inversion accuracy $\epsilon = \|\Gamma \cdot \Sigma - I\|_{\max}$, where I and $\|\cdot\|_{\max}$ are the identity and maximum matrix norm, respectively.

Analogously to the SNR computations, the Network and Detector instances save their respective quantities. The final two function calls simply print the contents of all the Detector instances inside the Network as well its own contents.

Further remarks: For the sake of simplicity, we omitted non-default function arguments in the example above. The Network class is designed to perform 'default'-benchmarking after setting all the necessary variables via `net.set_wf_vars` and `net.set_net_vars` without the need to pass further variables during the consecutive function calls. Nevertheless, certain functions give the user the option to tune the functionality of the code. In the following, we will present these options for the main GW benchmarking functions showcased in the example.

`net.setup_ant_pat_lpf_psd`: This function takes the following three arguments (default values) `F_lo` (`-np.inf`), `F_hi` (`np.inf`), and `psd_file_dict` (`None`). The first two are user-settable frequency cutoffs which truncate the frequency array, if they lie within the PSD's intrinsic frequency range. The third argument allows the user to specify PSD files that are not part of GWBENCH. It has to be passed as

```
psd_file_dict = {
    det_key1: {'psd_file': file1, 'is_asd': bool1}, ...
}
```

where the `det_key` are the exact keys that each Detector contains, the `file` are the relative paths to the PSD files, and the booleans `bool` tell the code whether the file contains PSDs S_n (`bool=0`) or amplitude spectral densities $\sqrt{S_n}$ (`bool=1`). The PSD files should be formatted like the txt-files in 'gwbench/noise_curves'. A caveat of using external PSD files is that the Network and Detector labels might not reflect this choice and will need manual changes. Fortunately, these can be done quite easily, if needed, in run time.

GWBENCH can naturally be used to just compute the antenna patterns, location phase factors, and PSDs of detectors as shown in the example script `COMPUTE_ANT_PAT_LPF_PSD.PY`.

`net.calc_det_responses_derivs_num`, `net.calc_wf_polarizations_derivs_num`: These functions calculate the derivatives of the detector responses and WF polarizations numerically via the NUMDIFFTOOLS package [46]. The numeric derivatives require four special arguments: the step size `step`, the differentiation scheme method, the differentiation order `order`, and the derivative order `n`. The respective default values in GWBENCH are `1e-7`, 'central', 2, and 1. We refer to the documentation of NUMDIFFTOOLS for further information. GWBENCH further allows the use of symbolic derivatives for certain waveforms via the SYMPY package. Their evaluation is faster, but requires a few extra steps compared to the numeric ones. Their usage is showcased in Section IV C, while Section V A compares the output of the numeric and symbolic differentiation methods.

`net.calc_snrs`, `net.calc_errors`, and `net.calc_sky_area_90`: These three functions have

a common argument `only_net` which tells the code whether to calculate the respective quantities just for the `Network` or also for each `Detector` within. The default is `0`, computing both network and detector quantities.

Besides, `net.calc_errors` takes two more arguments (default values) `cond_sup` (`1e15`) and `by_element` (`0`). The first determines the condition number supremum c^* that the code uses to assess whether a computed FIM Γ is well-conditioned ($c_\Gamma < c^*$). Passing `None` sets it to infinity, effectively making every FIM well-conditioned. The second argument tells the code whether to obtain a single inversion error ϵ for the entire FIM via the maximum norm (default) or n errors ϵ_i . n is the dimension of the FIM while each ϵ_i is the maximum of the elements of the i -th row and column combined. The single inversion error ϵ is equal to the maximum of the n errors.

C. Symbolic derivatives

Compute dictionaries of lambdified SYMPY derivatives: While numeric derivatives are computed and evaluated in the same, computationally expensive step, symbolic derivatives via SYMPY are first computed generically and then evaluated for a given set of arguments. The latter is faster than the numeric approach presented in Section IV B, but requires the generation of the so-called *lambdified* derivative functions ahead of time. In the following, we will showcase an example script that can handle this step: `GENERATE_LAMBDIFIED_FUNCTIONS.PY`.

The user has to specify the WF, the derivative variables, the detector locations of interest, and whether to take Earth's rotation into account. By default, the script is setup to (i) use the WF model `TaylorF2`, (ii) take derivatives with respect to chirpmass \mathcal{M} , symmetric mass ratio η , luminosity distance D_L , time and phase of coalescence t_c , ϕ_c , inclination angle ι , right ascension α , declination δ , and polarization angle ψ , (iii) use all locations available in `GWBENCH`, and (iv) include Earth's rotation.

Next, the code initializes a `Waveform` object and checks whether the derivative variables actually form a subset of the WF and antenna pattern arguments. The actual computation is then handled by

```
dr.generate_det_responses_sym(
    wf, deriv_syms_string, locs=locs, use_rot=use_rot)
```

which takes the `Waveform`, the derivative variables, the locations of interest, and the rotation setting.

The function generates two sets of dictionaries containing different *generic derivative expressions* stored as lambdified SYMPY functions. The first type contains the derivatives of the WF polarizations while the second stores the derivatives of the detector responses for the detector locations specified in the script. These dictionaries are then saved in a folder named `LAMBDIFIED_FUNCTIONS` using the `DILL` package. The output files contain one dictionary each and the file names are structured as

```
'par_deriv_WFM_{wf_model_name}_
  VAR_{variables}_DET_{location}.dat'
```

where `{wf_model_name}` and `{variables}` are set according to the values passed to `generate_det_responses_sym`. `{location}` is replaced by `pl.cr` in case of the WF polarizations.

Symbolic derivative evaluation for Fisher analysis: `SYM_GW_BENCHMARKING.PY` showcases how to load and evaluate the symbolic derivatives generated with `GENERATE_LAMBDIFIED_FUNCTIONS.PY` and how to use the `INJECTIONS` module to generate random samples of input parameters for the detector response evaluation (see Appendix F). The script is mimicked by `NUM_GW_BENCHMARKING.PY` which differs by computing the derivatives numerically; it can be seen as a more generic expansion of the example shown in Section IV B.

Most of the script simply prepares the benchmarking and hence we focus on the usage of symbolic derivatives, in order to avoid repetition. As before, the `Network` is the central hub and requires the same setup as shown in Section IV B to prepare the `Network` and `Detector` instances. In contrast to the earlier numeric example, the function call

```
net.calc_det_responses_derivs_num()
```

is replaced by

```
net.load_det_responses_derivs_sym()
net.calc_det_responses_derivs_sym()
```

which first loads the generated lambdified derivative functions and then evaluates them. This is all that is needed besides ensuring that the variables `wf_model_name`, `wf_other_var_dic`, `deriv_syms_string`, and `use_rot` are set to the same values as during the generation of the lambdified derivatives.

V. VALIDATING GWBENCH

In the following, we present benchmarking results obtained with `GWBENCH`. We compare numeric and symbolic derivatives and show their effects on the error estimates. We further present error estimates from various WF models for particularly interesting real events, namely GW170817 [2], GW190521 [47], and GW190814 [48].

A. Comparison of numeric and symbolic differentiation methods

`GWBENCH` contains both numeric and symbolic differentiation methods. The former can be used with all WF models, while the latter only works with some of the implemented WFs, as specified in Appendix B. In order to compare the two approaches for the purposes of GW benchmarking, we will compute the partial derivatives of the detector responses H and the error estimates for two WF models, `TaylorF2` (`tf2`) and `TaylorF2` with tidal effects (`tf2_tidal`) [49].

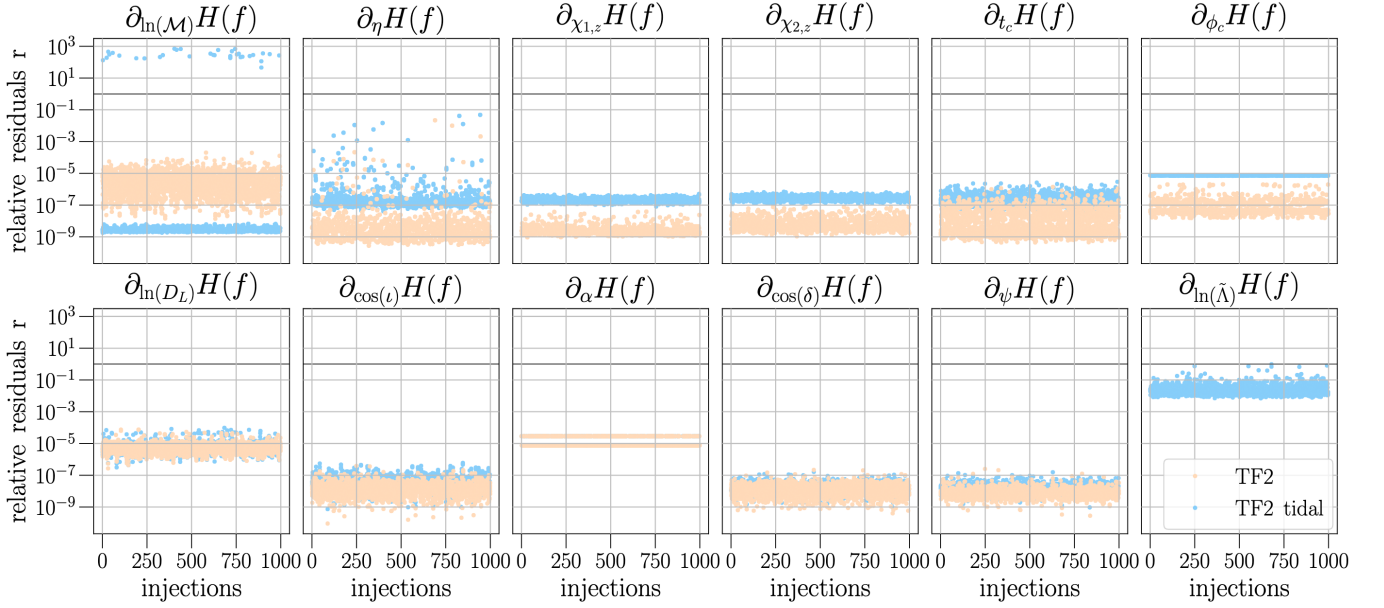


FIG. 1. The plots show the relative residuals r , see Equation (5.3), between the numeric and symbolic partial derivatives of the detector responses for 11 (12) input parameters and WF model `tf2` (`tf2_tidal`). The ~ 20 very poor residuals in the chirpmass derivatives correspond to ill-conditioned Fisher matrices and are therefore disregarded for further analysis.

Both WFs share the same set of input parameters, $(\mathcal{M}, \eta, \chi_{1,z}, \chi_{2,z}, D_L, t_c, \phi_c, \iota, \alpha, \delta, \psi)$, with the tidal WF further depending two tidal deformability parameter combinations $(\tilde{\Lambda}, \delta\tilde{\Lambda})$ [50]

$$\tilde{\Lambda} = \frac{8}{13} \left[(1 + 7\eta - 31\eta^2)(\Lambda_1 + \Lambda_2) + \sqrt{1 - 4\eta}(1 + 9\eta - 11\eta^2)(\Lambda_1 - \Lambda_2) \right], \quad (5.1)$$

$$\delta\tilde{\Lambda} = \frac{1}{2 \cdot 1319} \left[\sqrt{1 - 4\eta}(1319 - 13272\eta + 8944\eta^2)(\Lambda_1 + \Lambda_2) + (1319 - 15910\eta + 32850\eta^2 + 3380\eta^3)(\Lambda_1 - \Lambda_2) \right], \quad (5.2)$$

where the component tidal deformabilities Λ_1 and Λ_2 are defined as $\Lambda_i = \frac{2}{3}k_2C_i^5$ with Love number k_2 , compactness $C_i = \frac{m_i}{R_i}$, mass m_i , and radius R_i .

The partial derivatives are taken with respect to all available parameters except $\delta\tilde{\Lambda}$ for the tidal WF. The detector responses are evaluated for three detectors, each set to a 40km compact-binary optimized CE1 PSD, see Appendix D.

We performed this comparison for a total of 1000 random sets of input parameters for each WF. In both cases we chose the injections to be uniformly distributed in co-moving volume up to a redshift of $z = 0.5$ as well as over sky positions and orientation angles. The masses and spins are also sampled uniformly for both WFs albeit the ranges are chosen to resemble binary black hole or binary neutron star systems, respectively: $5 M_\odot \leq m_1, m_2 \leq 100 M_\odot$ and $-0.75 \leq \chi_{1,z}, \chi_{2,z} \leq 0.75$ for `tf2` and $1 M_\odot \leq m_1, m_2 \leq 2 M_\odot$ and $-0.05 \leq \chi_{1,z}, \chi_{2,z} \leq 0.05$ for `tf2_tidal`.

Figure 1 shows the relative residuals of all partial derivatives of the detector responses for both waveforms and all three

detectors. The residuals are defined via

$$r_x = \frac{\sqrt{\sum_i (\partial_x^{\text{num}} H(f_i) - \partial_x^{\text{sym}} H(f_i))^2}}{\sqrt{\sum_i (\partial_x^{\text{sym}} H(f_i))^2}} \quad (5.3)$$

where i runs over the input frequency array and $x \in \{\ln(\mathcal{M}), \eta, \chi_{1,z}, \chi_{2,z}, \ln(D_L), t_c, \phi_c, \cos(\iota), \alpha, \cos(\delta), \psi, \ln(\tilde{\Lambda})\}$.

The inclusion of tidal effects results in two trends for the relative residuals of the partial derivatives in Figure 1: The errors of the derivatives with respect to the so-called intrinsic parameters, $(\mathcal{M}, \eta, \chi_{1,z}, \chi_{2,z}, t_c, \phi_c, \tilde{\Lambda}, \delta\tilde{\Lambda})$, worsen but are also more tightly constrained, while the derivatives with respect to the extrinsic parameters $(D_L, \iota, \alpha, \delta, \psi)$ appear to not be affected. The only exceptions are the chirpmass and symmetric mass ratio derivatives, with the former showing improved residuals with tidal effects and the latter showing more scatter. The reason for the discrepancy in the behavior of the intrinsic and extrinsic derivatives is found in the correlation of the intrinsic parameters to each other, thus worsening the numeric derivatives when adding another intrinsic parameter, whereas the extrinsic parameters stay unaffected.

Overall, the partial derivatives appear to be well-behaved with relative residuals well below 10^{-4} . The tidal parameter derivatives perform the worst, but stay below an error of 10% for most of the samples. Finally, the ~ 20 very poor residuals in chirpmass derivatives actually correspond to ill-conditioned Fisher matrices and are therefore disregarded for further analysis.

Figure 2 shows the relative residuals

$$\tilde{r}_x = \left| \frac{\sigma_x^{\text{num}} - \sigma_x^{\text{sym}}}{\sigma_x^{\text{sym}}} \right| \quad (5.4)$$

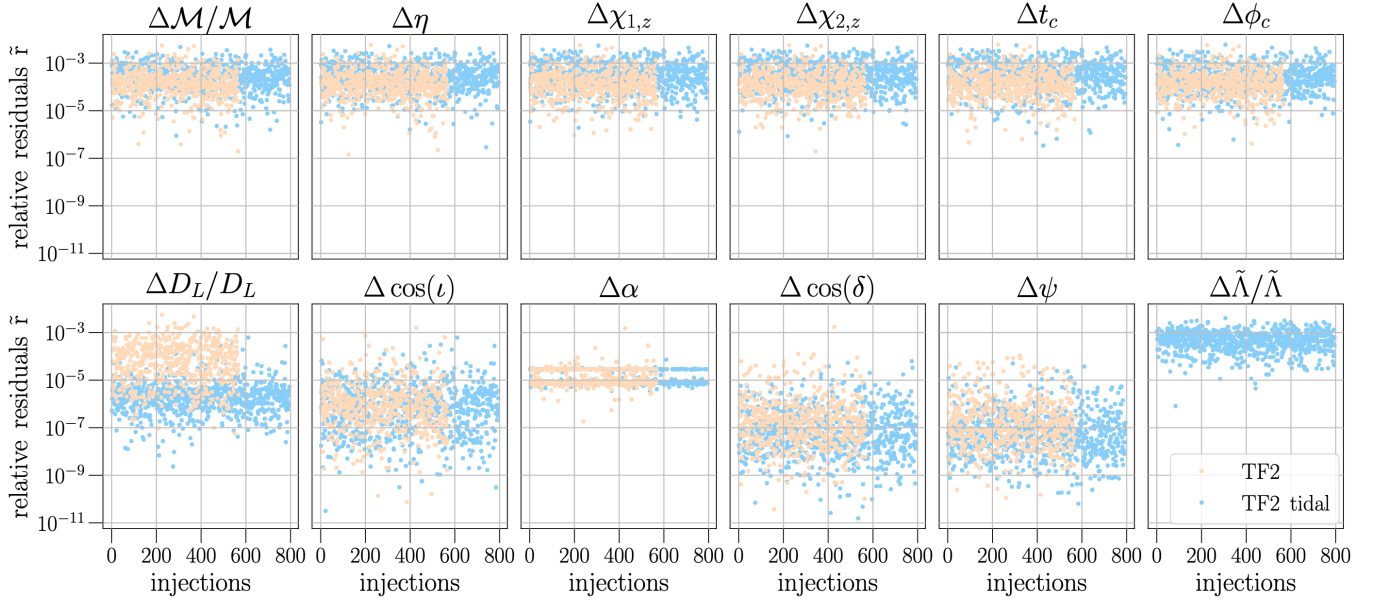


FIG. 2. The plots show the relative residuals \tilde{r} , see Equation (5.4), between the 1σ -error bounds, estimated via the FIF from numeric or symbolic derivatives, for 11 (12) input parameters and WF model `tf2` (`tf2_tidal`).

of the 1σ -errors bounds estimated from the FIF using the numeric and symbolic derivatives of the detector responses.

While the relative residuals on the parameter error estimates from Figure 2 do not show the actual discrepancy between the two derivative methods, they do show their effect on the final product of the Fisher analysis. It is important to note that the number of injections shown has decreased due to some parameter combinations yielding ill-conditioned Fisher matrices for which the further analysis is aborted. In fact, it appears that the inclusion of tidal effects has a stabilizing effect for the FIF, resulting in many more well-conditioned Fisher matrices. We remark that the mentioned differences in the behavior of the residuals between `tf2` and `tf2_tidal` could be simply a symptom of the different input parameter sets which we leave for a future study.

It appears that the correlations between intrinsic or extrinsic parameters smudges the differences in the numeric and symbolic derivatives within each of these parameter groups and the inclusion of tidal effects has little influence on the residuals. The only exception is presented in the case of the luminosity distance error bounds where the tidal WF resulted in improved errors. Overall, the relative residuals between the parameter error bounds, estimated with numeric and symbolic derivative methods, stay under 1% and mostly under 0.1%. Thus, we can use either approach confidently to perform the FIF.

B. Application to real events

GW170817 and GW190814 are among the loudest events observed by the LIGO and Virgo detectors so far with SNRs $\rho_{\text{GW170817}} = 32$ and $\rho_{\text{GW190814}} = 25$, respectively. These are exceptional candidates to check the FIF and GW benchmarking against. GW190521 is another interesting event representing

signals of average loudness with $\rho_{\text{GW190521}} = 14$ and very short duration as well as heavy binaries with merger- and ringdown-dominated signals. Neither of these events have well determined sky positions and binary orientations. We applied GWBENCH to 1000 realizations of the various angles while we fixed the masses, spins, and luminosity distances of the systems to the reported median values [2, 3, 47]. All three events were detected by three detectors located at the LIGO Hanford, LIGO Livingston, and Virgo sites. Since the actual sensitivities of these detectors during the detections are determined by the facilities, we used the respective PSDs for this analysis [51] and ran the FIF for 4 different WF models: `tf2_tidal` for GW170817, IMRPhenomD [52, 53] and IMRPhenomHM [4] for GW190521, and `tf2`, IMRPhenomD, and IMRPhenomHM for G190814.

We compare the reported values for the SNR ρ , the fractional error estimates of the chirpmass $\Delta M/M$ and luminosity distance $\Delta D_L/D_L$, as well as the 90%-credible sky area Ω to our benchmarking results. While this comparison contains only four quantities, we still perform the FIF with respect to 11 (GW190521 and GW190814) or 12 (GW170817) parameters, in order to not underestimate the error bounds. These 11 and 12 parameters are the same sets as in Section V A above for `tf2` and `tf2_tidal`, respectively. Besides, in order to allow for an easier comparison with the measured values we converted the fractional errors from the standard 1σ -output of the FIF to the respective 90% credible bounds.

The benchmarking posteriors for the 1000 realizations are presented in Figure 3 indicating that they capture the measured errors well for at least one of the WF models per event. The figure shows that `tf2_tidal` performs really well for an inspiral dominated, binary neutron star signal like GW170817. This does not hold for signals from the heavier binaries. For such systems, the error estimates from `tf2` do not capture

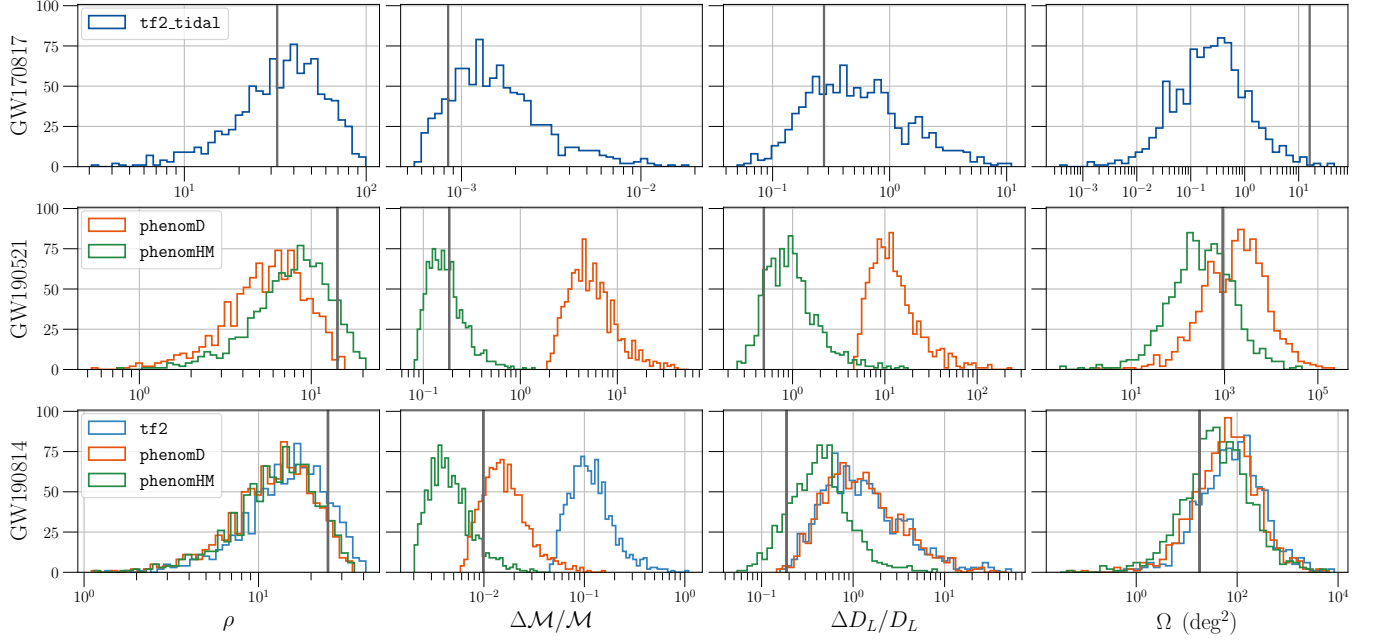


FIG. 3. The figure shows the histograms of four quantities (SNR ρ , 1σ -fractional error estimates of the chirpmass $\Delta M/M$ and luminosity distance $\Delta D_L/D_L$, and the 90%-credible sky area Ω) computed with `gwbENCH` for three real events (GW170817, GW190521, and GW190814). The histograms are generated from 1000 realizations of the sky positions and binary orientations while masses, spins, and luminosity distances are set to the measured values. The networks are set the same detector locations, LIGO Hanford, LIGO Livingston, and Virgo, and PSDs from the actual events. The vertical lines are the measured values from the respective events [2, 3, 47].

the measured values due to missed post-inspiral contributions (GW190814), while the FIF completely failed for a strongly merger- and ringdown-dominated signal (GW190521). In fact, for both of these systems it was necessary to use `IMRPhenomHM`, a WF with higher modes, and not just `IMRPhenomD` in order to fully capture the measured errors.

These findings are in line with the WFs used for the actual parameter estimation analyses of these events and they show that `gwbENCH` provides a consistent tool for the purposes of GW benchmarking.

VI. EXAMPLE APPLICATIONS

`gwbENCH` has already been applied in two works: [54, 55]. In [54] we examined the possibility to use dark sirens—GW sources without an electromagnetic counterpart—to resolve the tension in the measurement of the Hubble constant. In [55] we studied how multiband observations of GW signals with the space-based LISA and ground-based 3G observatories will open up new possibilities to conduct multiparameter tests of general relativity in the line of [56].

A. “Dark sirens to resolve the Hubble-Lemaître tension”

We examined the prospect to use dark sirens to perform precision measurements of the Hubble constant and thus provide a GW-assisted method to resolve the Hubble-Lemaître

tension. The proposed method makes use of the potential of future observatories to measure sky positions of close-by dark sirens well enough to pin-point the host galaxy of the GW event. This provides two independent measurements, the distance from the GW signal and the galaxy’s redshift from electromagnetic follow-up observations, which compound to estimate the Hubble constant.

We simulated three populations of dark sirens: one resembled binary black holes from the GWTC-1 catalog [3], the second focused on the heavy sub-population of such BBHs with component masses $m_1, m_2 > 25 M_\odot$, while the third was GW190814-like [48]. The GWTC-1 catalog summarizes the detections from the first two observing runs of the LIGO and VIRGO detectors and GW190814 was the most asymmetric binary observed to date.

For each population we performed the Fisher analysis in four networks containing three possible detector technologies of the future (‘Advanced+’, ‘Voyager’, and 3G). In order to leverage the sensitivities of such future networks we used the `LALSIMULATION` WF `IMRPhenomHM` [4] which also models subdominant, higher-order spherical harmonic modes beyond the quadrupole. These higher modes improve the distance measurement by breaking the degeneracy between the luminosity distance and the inclination angle of the binary orbit to the line of sight, thus ultimately yielding better measurements of the Hubble constant.

Using `gwbENCH` we performed the FIF with numeric derivatives for 10^4 binaries per population. We estimated the number of detections to expect from the studied networks that yield pre-

cise measurements of the dark siren’s sky position and propagated the error bounds on the luminosity distance measurement to estimate the accuracy of a Hubble constant measurement. We showed that, if redshift errors are well controlled, dark siren observations will yield $\lesssim 2\%$ -accurate Hubble constant measurements already in the Advanced+ era and thus resolve the Hubble-Lemaître tension.

B. “Multiparameter tests of general relativity using multiband gravitational-wave observations”

Parameterized post-Newtonian tests [56] present a crucial resource to perform theory-agonistic tests of general relativity which can probe generically potential deviations of GW signals from Einstein’s theory. This class of tests is especially important when verifiable GW predictions from alternate theories of gravity are sparse. The tests are based on modifications to the expansion coefficients in the post-Newtonian approximation to the WFs emitted by compact binary coalescences, such that these deviations vanish if general relativity is correct. Unfortunately, the current tests are handicapped by the strong correlations between the introduced deviation parameters. Therefore, parameterized post-Newtonian tests are limited to single-coefficient modifications for now. We showed that the combination of the information present in the low-frequency LISA and high-frequency 3G bands breaks this degeneracy. Thus such multiband observations allow for true multiparameter tests of general relativity.

In our study we examined stellar mass binary black hole coalescences. Their inspiral signals will last several years in the LISA band ($\sim 0.1 - 100$ mHz) before they reach the 3G band (\sim Hz-kHz) where they finally merge. Unfortunately, these signals, while extremely loud in 3G networks, will be faint to non-visible in LISA, making the ‘joint’ observation a difficult task. The issue lies in the detection methodology for such quiet signals. The current state-of-the-art are blind, matched filtering searches [57, 58] without a-priori knowledge of the GW signal. Such blind searches require GW template banks which cover a large volume in the parameter space. Thus, the sizes of the banks become computationally infeasible for the signals of interest in the LISA band [59].

Fortunately, we can leverage the high-fidelity detections with 3G detectors to dig out these quiet signals from LISA’s archival data. In contrast to a blind search the 3G detection confirms the existence of the signal we are searching for and further provides information about it, allowing for the generation of signal-specific template banks that decrease the computational cost immensely. This is enabled in two-ways: A 3G network will estimate all WF parameters except chirpmass and symmetric mass ratio to better precision than LISA could, thus decreasing the parameter dimension of the template bank to two and fixing the other parameters to the 3G measurement. The search volume can be further narrowed down to within the error bounds estimated from the 3G detection for both chirpmass and symmetric mass ratio.

Using `GWBENCH`, we tackled the question of feasibility to search the archival LISA data following a 3G detec-

tion, strengthening our proposal to perform multiband multiparameter tests of general relativity. For this purpose we generated a set of 500,000 binary black holes up to a redshift of $z = 10$. Roughly 200 of these binaries should be visible in LISA with an $\text{SNR} \geq 4$ which we set as the threshold for visibility in the archival search. `GWBENCH` allowed us to estimate the SNR and 1σ error bounds on the WF parameters for a network consisting of one Einstein Telescope and two 40 km, CE2 detectors in compact binary optimization.

Given the LISA SNR ρ_{LISA} and 3G errors on chirpmass σ_{M_c} and symmetric mass ratio σ_η , we used `GWBENCH` to calculate the detector-dependent volume V via the metric g [60, 61]

$$g = \rho_{\text{LISA}}^{-2} \det \left(\langle \partial_x H, \partial_y H \rangle_{x,y \in \{M_c, \eta\}} \right) \quad (6.1)$$

as

$$V = \int_{M_c - 2\sigma_{M_c}}^{M_c + 2\sigma_{M_c}} dM_c \int_{\eta - 2\sigma_\eta}^{\eta + 2\sigma_\eta} d\eta \sqrt{g}. \quad (6.2)$$

The inner product in the definition of the metric is taken with respect to the LISA PSD. Finally, the number of templates N is given by the ratio of the total volume to the volume of the error ball around each template for a given minimal match mm

$$N = \frac{V}{1 - mm}. \quad (6.3)$$

Using $mm = 0.95$, we found that such targeted searches of LISA’s archival data following the detection of a binary black hole merger in a network of 3G detectors should allow for template bank sizes of the order $10^3 - 10^4$. This is substantially less than the value of 10^{12} predicted before [59]. Ultimately, `GWBENCH` enabled us to check the feasibility of multibanding to perform multi-parameter tests of general relativity by providing the tools to calculate estimates of both the 3G errors bounds and the LISA template numbers.

VII. SUMMARY

In this work we presented `GWBENCH`, a `PYTHON` package for fast and straightforward applications of the Fisher information formalism for the purposes of GW benchmarking. The package is written with the usage for detector networks in mind. Thus, it is structured around the `Network` class which acts as a hub for user interaction and facilitates all the possible computations. The package gives easy access to a variety of GW benchmarking quantities such as the frequency-domain WF polarizations, antenna pattern functions and location phase factors as well as noise PSDs for various detector locations and technologies, frequency-domain detector responses, SNRs, Fisher and covariance matrices, and the product of the FIF, the 1σ error bounds for input parameters of choice.

There are two types of WFs available, both of which support numeric differentiation via the `NUMDIFFTOOLS` package: `LAL` WFs as well as those implemented `GWBENCH`. The latter further support symbolic derivatives via `SYMPY` which are faster and

more accurate. The inclusion of LAL WF support is very important as it gives access to a host of WF models that are well tested and commonly used in the literature. `GWBENCH` contains nine existing, planned, or fiducial detector locations and 23 different detector technologies ranging from aLIGO to various CE sensitivity curves. The addition of user-defined locations and technologies is also possible. Another specialty of this package is the inclusion of the effects of Earth’s rotation in the antenna patterns and detector responses, and thus the FIF. This is particularly important for long-lived GW signals such as from binary neutron stars.

`GWBENCH` is and has been used for several research projects of which we presented two that are in public already. In both cases, `GWBENCH` allowed us to generate and calculate parameter errors and even template numbers for a matched filtered search for large numbers of sources and detector networks. `GWBENCH` represents a unique code that implements the FIF and GW benchmarking in an easy-to-use manner for a wide range of problems, WFs, and network options and allows for straightforward application in large-scale simulations for improved statistics of the scientific claims.

ACKNOWLEDGMENTS

I thank Bangalore Sathyaprakash, Anuradha Gupta, Patrick Godwin, and everyone in the Cosmic Explorer Project for helpful comments and discussions during the development of `GWBENCH`. I further thank Kevin Kuns, Varun Srivastava, Evan Hall, Matthew Evans, and Stefan Ballmer for providing the sensitivity curves used in `GWBENCH`. I also thank all front line workers combating the CoVID-19 pandemic and those maintaining ordinary life without whose support this work would not have been possible. I acknowledge the support by NSF grant PHY-1836779. Computing resources for the development and testing of this code were provided by the Pennsylvania State University.

Appendix A: Network and Detector classes

GW detector networks consist, as per name, of a number of detectors that work in tandem to observe GWs to improve signal strength, sky coverage, and parameter estimation. Leaning on this understanding, the `Network` class is designed as a GW benchmarking hub for a chosen set of detectors. The class structure allows for straightforward handling of the relevant quantities and network methods and thus provides the user with tools to load, calculate, and manipulate quantities like waveforms, SNRs, or errors estimates.

The `Detector` class is written with similar syntax and methodology as the `Network` class. This is very natural because network quantities like SNR or error estimates are handled in the same manner as the respective single detector ones. This choice allows for clearer codes and faster development, but also better understanding of both classes, which helps when using `Network` objects. Thus, Table I compares the *instance variables* of both classes side-by-side. The top section of the

table lists the variables which are set by the user and tell the `Network`

- the label of the `Network` and what location and technology to use for a `Detector` instance,
- which `Detector` instances to initialize,
- what frequency array and injection parameters to use for function evaluation, and with respect to which parameters to take derivatives for error estimation via FIF,
- what `Waveform` to initialize,
- which parameters x to convert to $\cos(x)$ or $\ln(x)$ to estimate errors on the latter, and whether to take Earth’s rotation into account.

The bottom section shows the variables which can be loaded and computed with instance methods based on the user-set variables:

- Detector-specific quantities like PSDs, antenna patterns, and location phase factors are loaded and stored in each `Detector` instance.
- The WF polarizations and the respective derivative dictionaries are detector-agnostic and saved in the `Network`.
- Each `Detector` handles the respective detector response and derivative dictionaries.
- The detector and network SNRs (and their squares) are stored in the respective instances, where each `Detector` also saves the integrand of the square SNR.
- Each detector and the network contain their respective copy of the FIM, its condition number, a well-conditioned flag, the covariance matrix, the inversion error, and an error dictionary containing the 1σ errors extracted from the covariance matrix.

Appendix B: Implemented waveform models and the `Waveform` class

`GWBENCH` handles WF selection and evaluation within the `Waveform` class. The available WFs are listed in Table II together with their labels, their input parameters, and whether they allow for numeric or symbolic differentiation. One of the strong suites of `GWBENCH` is the implementation of WF models from LAL in the `Waveform` class and the capability to use them for the FIF with numeric derivatives. The class contains five instance variables

- `.wf_model_name`: internal name of the WF model,
- `.wf_other_var_dic`: extra input parameters,
- `.wf_syms_string`: string containing the basic parameters (space-separated),

TABLE I. Network vs Detector variables.

	Network	Detector
<i>set by user:</i>		
labels	<code>.label</code> (label to initialize network)	<code>.det_key</code> , <code>.tec</code> , <code>.loc</code> (full detector key, technology and location labels)
detectors	<code>.detectors</code> , <code>.det_keys</code> (list of Detector objects and detector keys)	—
global quantities	<code>.f</code> , <code>.inj_params</code> , <code>.deriv_syms_string</code> , <code>.deriv_variables</code> (frequency array, injection parameters, derivative parameters string and list)	<code>.f</code> (truncated frequency array)
waveform	<code>.wf</code> (Waveform object)	—
analysis settings	<code>.conv_cos</code> , <code>.conv_log</code> , <code>.use_rot</code> (lists of parameters x to convert to $\cos(x)$, $\ln(x)$, consider Earth's rotation)	—
<i>loaded or calculated by network methods:</i>		
detector specific quantities	—	<code>.psd</code> , <code>.fp</code> , <code>.fc</code> , <code>.flp</code> (detector PSD, antenna patterns, location phase factor)
waveform polarizations	<code>.hfp</code> , <code>.hfc</code> , <code>.del_hfpc</code> , <code>.del_hfpc_expr</code> (plus and cross polarizations, derivatives dictionary, SYMPY expressions dict)	—
detector responses	—	<code>.hf</code> , <code>.del_hf</code> , <code>.del_hf_expr</code> (detector response, derivatives dictionary, SYMPY expressions dict)
SNR	<code>.snr</code> , <code>.snr_sq</code> (SNR, SNR square)	<code>.snr</code> , <code>.snr_sq</code> , <code>.d_snr_sq</code> (SNR, SNR square, SNR square integrand)
error quantities	<code>.fisher</code> , <code>.cond_num</code> , <code>.wc_fisher</code> , <code>.cov</code> , <code>.inv_err</code> , <code>.errs</code> (Fisher information matrix, Fisher condition number, well conditioned boolean, covariance matrix, inversion error, the parameter errors)	<code>.fisher</code> , <code>.cond_num</code> , <code>.wc_fisher</code> , <code>.cov</code> , <code>.inv_err</code> , <code>.errs</code> (Fisher information matrix, Fisher condition number, well conditioned boolean, covariance matrix, inversion error, the parameter errors)

TABLE II. The available WFs are presented here, together with their labels, their input parameters, and whether they allow for numeric or symbolic differentiation. GWBENCH uses the same labeling convention for 'approximant' in the LAL WFs as specified in LALSIMULATION. Check the *Approximant*-list for frequency-domain approximants, implemented in lalsimulation, under *Enumerations* at https://lscsoft.docs.ligo.org/lalsuite/lalsimulation/group__l_a_l_sim_inspiral__h.html.

Waveforms	Waveform label	Input parameters	Other parameter dictionary
<i>LAL WFs — only numeric differentiation</i>			
BBH	'lal_bbh'	'f Mc eta chi1x chi1y chi1z chi2x chi2y chi2z DL tc phic iota'	{'approximant':name_string}
BNS	'lal_bns'	'f Mc eta chi1x chi1y chi1z chi2x chi2y chi2z DL tc phic iota lam_t delta_lam_t'	{'approximant':name_string}
<i>Coded WFs — numeric and symbolic differentiation</i>			
TaylorF2	'tf2'	'f Mc eta chi1z chi2z DL tc phic iota'	None
TaylorF2 + tidal	'tf2_tidal'	'f Mc eta chi1z chi2z DL tc phic iota lam_t delta_lam_t'	None

- `.hfpc_np`: NUMPY function,
- `.hfpc_sp`: SYMPY function,

and few methods of which two are of particular interest to the user:

- `.get_sp_expr()`: load the SYMPY function to obtain a symbolic expression which can be manipulated,

- `.eval_np_func(f, inj_params)`: evaluates the NUMPY function for the given frequency array `f` and injection parameters `inj_params`.

(The injection parameters `inj_params` can be either provided as a dictionary with keys equal to the parameters defined in `.wf_syms_string` or as a list with the same ordering given by `.wf_syms_string`.)

Only the `wf_model_name` and `wf_other_var_dic` are

TABLE III. The available detector locations are presented together with the respective labels and detector angles (longitude α_d , latitude β_d , and orientation of the y-arm with respect to due East γ_d). The five locations H, L, V, K, I are chosen in accordance with the implementation in LAL (https://lscsoft.docs.ligo.org/lalsuite/lal/_l_a_l_detectors_8h_source.html). The four locations E, C, N, and S are fiducial example sites and do not represent candidates under active consideration.

Label	Location	angles (rad)		
		α_d	β_d	γ_d
H	LIGO Hanford (Washington, USA)	-2.084060	0.810795	-2.513290
L	LIGO Livingston (Louisiana, USA)	-1.584310	0.533423	-1.261590
V	Virgo (Cascina, Italy)	0.183338	0.761512	2.802430
K	KAGRA (Kamioka, Japan)	2.394200	0.632682	2.087480
I	LIGO India (Hingoli, India)	1.334013	0.248418	1.570800
E	Einstein Telescope (Cascina, Italy)	0.183338	0.761512	2.802430
C	Cosmic Explorer (main) (Idaho, USA)	-1.969170	0.764918	0.000000
N	Cosmic Explorer North (New Mexico, USA)	-1.858430	0.578751	-1.047200
S	Cosmic Explorer South (New South Wales, Australia)	2.530730	-0.593412	0.785398

needed to fully initialize a `Waveform` instance:

```
from gwbench import wf_class

wf = wf_class.Waveform(
    wf_model_name = wf_model_name,
    wf_other_var_dic = wf_other_var_dic)
```

The LAL WF models do not provide any of the aforementioned symbolic functionality, enabled by `SYMPY`, as this requires a direct implementation of the WF model to ensure proper `SYMPY` function calls.

Appendix C: Implemented detector locations - antenna patterns and location phase factor

Table III summarizes the nine available detector locations in `GWBENCH` together with the respective labels used in the code, while Figure 4 presents their spread across the world map. There are five 2G detector sites at LIGO Hanford (Washington, USA), LIGO Livingston (Louisiana, USA), VIRGO (Cascina, Italy), KAGRA (Kamioka, Japan), and LIGO India (Hingoli, India) as well as four fiducial sites for the 3G detectors. The Einstein Telescope is set to the same coordinates as VIRGO, while the three Cosmic Explorer locations Main, North, and South are set to sites in Idaho (USA), New Mexico (USA), and New South Wales (Australia)⁴.

The computation of the antenna patterns F_+ , F_\times and location phase factors F_{lp} for these locations is implemented in the two modules `ANTENNA_PATTERN_NP.PY` and `ANTENNA_PATTERN_SP.PY` which differ in their intended usage: the former is used to calculate the respective quantities directly whereas the latter is required for the generation of the symbolic derivatives via `SYMPY`.

The core concepts for a single detector are demonstrated in [32], whereas [62] outlines the more intricate methods required

for the analysis of a network of detectors where calculations are carried out in a universal frame centered at Earth's center. In either case, F_+ , F_\times , and F_{lp} depend on a few signal-specific quantities: right ascension α , declination δ , and polarization angle ψ . In a network, these functions further depend on the arrival time t_E of the signal at Earth's center as well as three detector- and location-specific angles: the longitude α_d and latitude β_d of the detector site as well as the angle γ_d of the detector's y-arm with respect to due East⁵.

All these considerations omit the effects of Earth's rotation on the antenna patterns and location phases factors. These effects are negligible for short-lived, transient signals lasting only a few minutes or less. They cannot be neglected for 3G detectors which will see signals that can be up to a few days long. Hence, `GWBENCH` contains the functionality to take Earth's rotation, simplified as a constant circular rotation with a period of one day, into account which follows the calculations detailed in [33, 34].

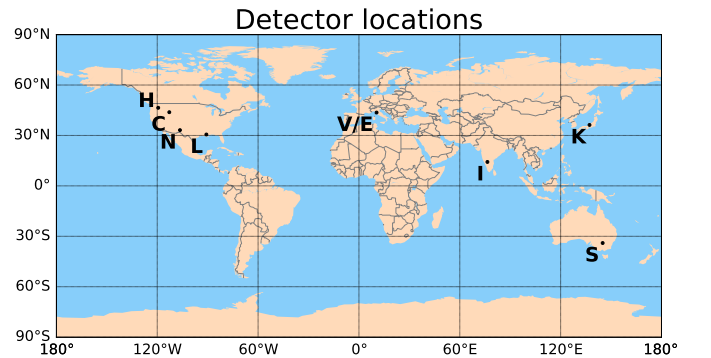


FIG. 4. The available detector locations shown on the world map.

⁴ The four fiducial 3G detector locations are example sites and do not represent candidates under active consideration.

⁵ Since the Einstein Telescope consists of three V-shaped detectors ET1, ET2, and ET3, that form an equilateral triangle, γ_d is fiducially set to correspond to ET1. The fixed geometry allows the calculation of the detector quantities for all three detectors.

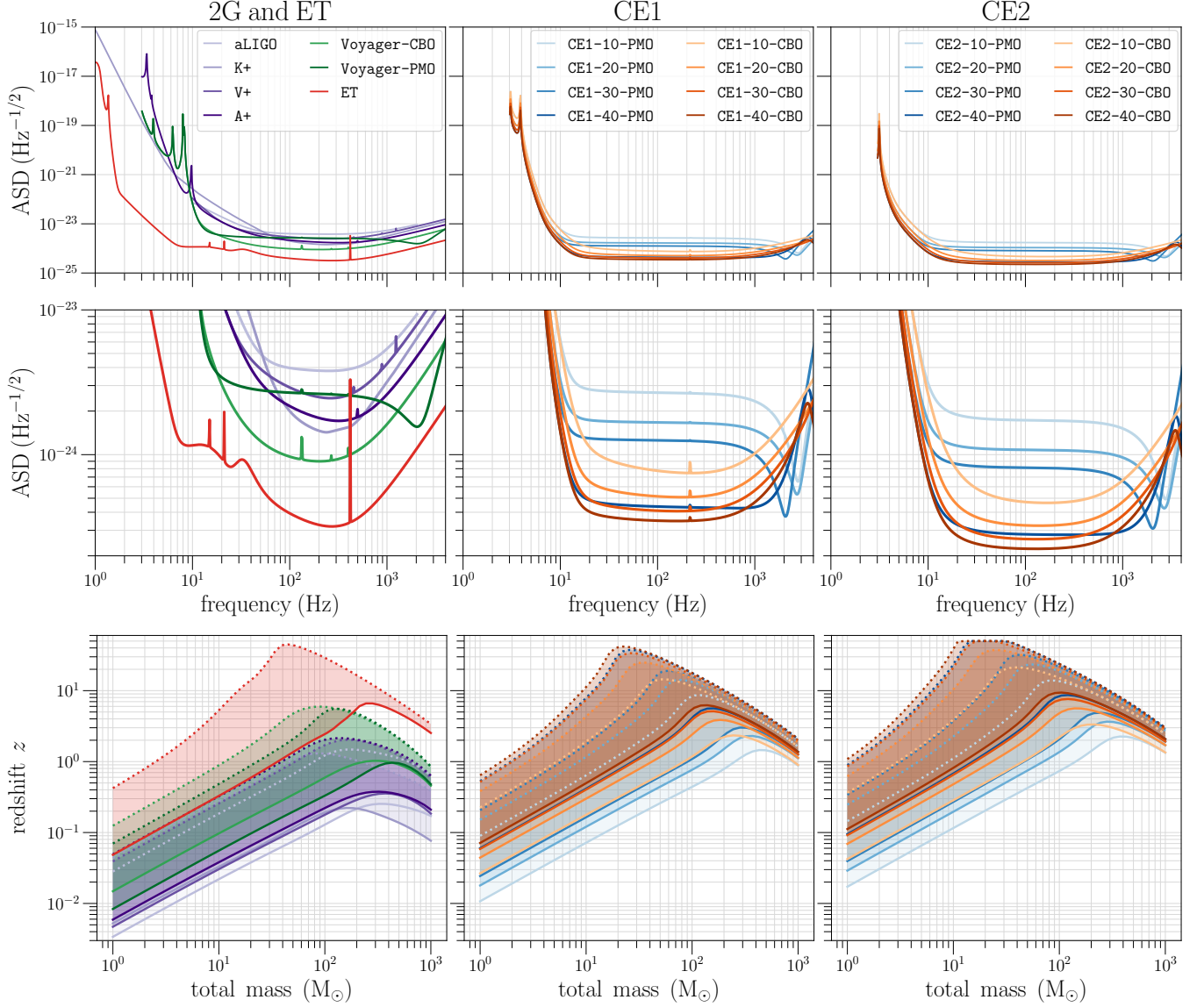


FIG. 5. The *top* shows the amplitude spectral densities (ASD) $\sqrt{S_n(h)}$ available in *GWBENCH*, see Figure 6, as functions of the frequency between 1 and 4096 Hz. The *bottom* presents the observable redshifts for equal-mass binaries at SNR 100 (solid) and 12 (dotted) as functions of the total binary mass between 1 and 1000 M_\odot (in the source frame). The systems are assumed to be optimally orientated for an L-shaped detector with the respective ASD. The SNRs were obtained for the LAL WF *IMRPhenomHM*. The shaded regions show the respective ranges for events with SNRs between 12 and 100.

Appendix D: Implemented detector technologies - detector PSDs

Figures 6 and 5 show the 23 available PSDs [63] in *GWBENCH*. The former is a graphical summary presenting the hierarchy of these PSDs in terms of detector generation (2G and 3G) and design concepts (Advanced+ vs Voyager vs ET vs CE and more) while the latter shows the amplitude spectral densities $\sqrt{S_n(h)}$ as functions of frequencies. Figure 5 further presents the observable redshift ranges for equal-mass binaries with total mass between 1 and 1000 M_\odot (source frame), if observed with SNRs between 12 and 100. Table IV presents the respective label and key options for these PSDs.

Appendix E: Derivative dictionaries

GWBENCH obtains the partial derivatives of the WF polarizations and detector responses either numerically or symbolically using the *NUMDIFFTOOLS* or *SYMPY* packages, respectively. The former calculates the evaluated derivatives directly which is computationally expensive but applicable to most WFs. *SYMPY* on the other hand works with symbolic expressions that require modifications to the WF source code. In return they enable the analytic computation of generic derivative expressions which can be stored in the form of *lambdified functions* for fast evaluation in run time.

TABLE IV. The available detector PSDs are presented together with the respective labels and internal keys as used by GWBENCH. CBO stands for compact-binary optimized and PMO for post-merger optimized. The former PSD will be tuned towards increased sensitivity at low frequencies, while the latter is geared towards high frequencies. There are two examples illustrating the nomenclature of the CE configurations.

Label	Internal keys	PSD
-	aLIGO	aLIGO
+	A+, V+, K+	A+ (adV+/KAGRA+ for V/K location)
vc	Voyager-CBO	Voyager, CBO
vp	Voyager-PMO	Voyager, PMO
E	ET	ET-D (same as location)
sLo	<s>-<L>-<o>	CE configurations (see below)

CE configurations - <s>-<L>-<o>

	stage s	length L	optimizations o
Label option	i / a	1 / 2 / 3 / 4	c / p
Key option	CE1 / CE2	10 / 20 / 30 / 40	CBO / PMO
PSD setting	CE1 / CE2	(10 / 20 / 30 / 40) km	CBO / PMO

CE configurations - Examples

Label	Internal key	PSD
i2p	CE1-20-PMO	CE1, 20 km, PMO
a4c	CE2-40-CBO	CE2, 40 km, CBO

The evaluated partial derivatives are stored in dictionaries which are structured as follows

```
{'del_variable1_hf': <numpy array>,
 'del_variable2_hf': <numpy array>,
 ... }
```

in case of the detector responses and

```
{'del_variable1_hfp': <numpy array>,
 'del_variable1_hfc': <numpy array>,
 'del_variable2_hfp': <numpy array>,
 'del_variable2_hfc': <numpy array>,
 ... }
```

for the WF polarizations. These dictionaries have the same structure in case of the symbolic derivative expressions, but store lambdified SYMPY functions instead of NUMPY arrays. Further, they contain two extra keys, 'variables' and 'deriv_variables', that store the input parameters and the differentiation variables.

Appendix F: INJECTIONS module

The module INJECTIONS contains functions to randomly sample input parameters appropriate for GW problems: chirpmass

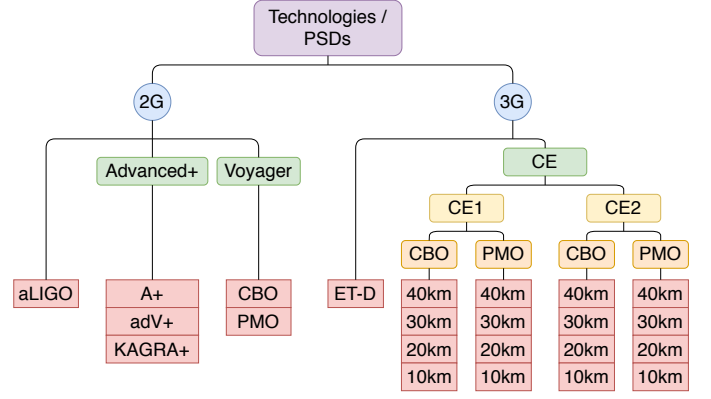


FIG. 6. Detector technologies/PSDs available in GWBENCH. The included 2G PSDs encompass aLIGO as well as the planned Advanced+ and proposed Voyager upgrades. The 3G PSDs encompass the ET-D curve for the Einstein Telescope and various Cosmic Explorer configurations, subdivided in the CE1 and CE2 stages. CBO and PMO stand for compact-binary or post-merger optimized, i.e. focus on low- or high-frequency sensitivity, respectively.

and symmetric mass ratio, binary component spins, sky location and binary orientation angles, as well as redshifts and luminosity distances. The inputs of the sampler functions are the same across the board: dictionaries specifying details of the parameter space to sample, the number of injections `num_injs` to sample, and the seed value `seed` for the random number generator. In the following we show the usage of these functions and explain what the respective dictionaries contain.

Mass sampler: The chirpmass and symmetric mass ratio sampling is handled by `mass_sampler`:

```
from gwbench import injections
```

```
Mcs, etas = injections.mass_sampler(
    mass_dict, num_injs, seed)
```

The `mass_dict` contains three definite keys:

- 'dist': specifies the mass distribution (values: 'gaussian', 'power', 'power_uniform', and 'uniform').
- 'mmin': specifies the minimum mass.
- 'mmax': specifies the maximum mass.

The Gaussian and power-law distributions need further inputs, namely 'mean' and 'sigma' or 'alpha', respectively. The first two specify the mean and standard deviation for the Gaussian distribution while the 'alpha' is the power-law index.

Spin sampler: The binary spin components sampling is handled by `spin_sampler`:

```
chilx, chily, chilz, chi2x, chi2y, chi2z =
    injections.spin_sampler(spin_dict, num_injs, seed)
```

The `spin_dict` contains four keys.

- 'geom': specifies the geometry (values: 'cartesian' and 'spherical').
- 'dim': specifies spin dimension (values: 1 and 3; one-dimensional spin sampling disregards 'geom' and samples using Cartesian geometry; further 1 returns zeroes for the x- and y-components to sample aligned injections).
- 'chi_lo': specifies the minimum spin value (smallest spin value in each dimension for 'cartesian' geometry or smallest spin magnitude for 'spherical' geometry).
- 'chi_hi': specifies the maximum spin value (largest spin value in each dimension for 'cartesian' geometry or largest spin magnitude for 'spherical' geometry).

Angle sampler: The sky location and orientation angles sampling is handled by `angle_sampler`:

```
iotas, ras, decs, psis = injections.angle_sampler(
    num_injs, seed)
```

Redshift and luminosity distance sampler: The redshift and luminosity distance sampling is handled by `redshift_lum_distance_sampler`:

```
zs, DLs = injections.redshift_lum_distance_sampler(
    cosmo_dict, num_injs, seed)
```

The `cosmo_dict` contains three definite keys

- 'sampler': specifies the redshift sampling method (values: 'uniform', 'uniform_comoving_volume_inversion' and

'uniform_comoving_volume_rejection'; the inversion method is faster, while the rejection method is more accurate, especially for very jagged redshift distributions).

- 'zmin': specifies the minimum redshift.
- 'zmax': specifies the maximum redshift.

By default the code samples redshifts from the redshift distribution `astropy.cosmology.Planck18` provided in the `ASTROPY` package. The user can change this behavior by adding three further keys to the `cosmo_dict` whose values are then passed to `astropy.cosmology.LambdaCDM`:

- 'H0': specifies Hubble constant.
- 'Om0': specifies the mass density $\Omega_{m,0}$ at the current time.
- 'Ode0': specifies dark energy density $\Omega_{\Lambda,0}$ at the current time.

Injection parameter sampler: `INJECTIONS` further contains a function that combines the four other samplers into one function call: `injections.CBC_params_redshift`. Hence it depends on the same input as the previous four methods:

```
data = injections.injections_CBC_params_redshift(
    cosmo_dict, mass_dict, spin_dict, redshifted,
    num_injs, seed, file_path)
```

The two additional inputs, `redshifted` and `file_path`, control whether the sampled masses are already redshifted (1) according to the sampled redshifts or not (0) as well as if the sampled data should be stored in a file at the specified path (default is None), respectively.

-
- | | |
|---|--|
| <p>[1] LIGO SCIENTIFIC, VIRGO collaboration, <i>Observation of Gravitational Waves from a Binary Black Hole Merger</i>, <i>Phys. Rev. Lett.</i> 116 (2016) 061102 [1602.03837].</p> <p>[2] LIGO SCIENTIFIC, VIRGO collaboration, <i>GW170817: Observation of Gravitational Waves from a Binary Neutron Star Inspiral</i>, <i>Phys. Rev. Lett.</i> 119 (2017) 161101 [1710.05832].</p> <p>[3] LIGO SCIENTIFIC, VIRGO collaboration, <i>GWTC-1: A Gravitational-Wave Transient Catalog of Compact Binary Mergers Observed by LIGO and Virgo during the First and Second Observing Runs</i>, <i>Phys. Rev. X</i> 9 (2019) 031040 [1811.12907].</p> <p>[4] L. London, S. Khan, E. Fauchon-Jones, C. García, M. Hannam, S. Husa et al., <i>First higher-multipole model of gravitational waves from spinning and coalescing black-hole binaries</i>, <i>Phys. Rev. Lett.</i> 120 (2018) 161102 [1708.00404].</p> <p>[5] R. Cotesta, A. Buonanno, A. Bohé, A. Taracchini, I. Hinder and S. Ossokine, <i>Enriching the Symphony of Gravitational Waves from Binary Black Holes by Tuning Higher Harmonics</i>, <i>Phys. Rev. D</i> 98 (2018) 084028 [1803.10701].</p> <p>[6] LIGO SCIENTIFIC collaboration, <i>Advanced LIGO</i>, <i>Class. Quant. Grav.</i> 32 (2015) 074001 [1411.4547].</p> | <p>[7] VIRGO collaboration, <i>Advanced Virgo: a second-generation interferometric gravitational wave detector</i>, <i>Class. Quant. Grav.</i> 32 (2015) 024001 [1408.3978].</p> <p>[8] KAGRA collaboration, <i>Interferometer design of the KAGRA gravitational wave detector</i>, <i>Phys. Rev. D</i> 88 (2013) 043007 [1306.6747].</p> <p>[9] C. for Indian Initiative in Gravitational-wave Observations (IndIGO), <i>Ligo-india, proposal</i>, (2011), https://dcc.ligo.org/LIGO-M1100296/public.</p> <p>[10] LSC, <i>Instrument science white paper</i>, (2016), https://dcc.ligo.org/LIGO-T1600119/public.</p> <p>[11] KAGRA, LIGO SCIENTIFIC, VIRGO collaboration, <i>Prospects for Observing and Localizing Gravitational-Wave Transients with Advanced LIGO, Advanced Virgo and KAGRA</i>, <i>Living Rev. Rel.</i> 21 (2018) 3 [1304.0670].</p> <p>[12] eLISA collaboration, <i>The Gravitational Universe</i>, [1305.5720].</p> <p>[13] M. Maggiore et al., <i>Science Case for the Einstein Telescope</i>, <i>JCAP</i> 03 (2020) 050 [1912.02622].</p> <p>[14] LIGO collaboration, <i>A Cryogenic Silicon Interferometer for Gravitational-wave Detection</i>, <i>Class. Quant. Grav.</i> 37 (2020)</p> |
|---|--|

- 165003 [2001.11173].
- [15] M. Punturo et al., *The Einstein Telescope: A third-generation gravitational wave observatory*, *Class. Quant. Grav.* **27** (2010) 194002.
- [16] M. Punturo et al., *The third generation of gravitational wave observatories and their science reach*, *Class. Quant. Grav.* **27** (2010) 084007.
- [17] D. Reitze et al., *Cosmic Explorer: The U.S. Contribution to Gravitational-Wave Astronomy beyond LIGO*, *Bull. Am. Astron. Soc.* **51** (2019) 035 [1907.04833].
- [18] C. Cutler and E. E. Flanagan, *Gravitational waves from merging compact binaries: How accurately can one extract the binary's parameters from the inspiral wave form?*, *Phys. Rev. D* **49** (1994) 2658 [gr-qc/9402014].
- [19] E. Poisson and C. M. Will, *Gravitational waves from inspiraling compact binaries: Parameter estimation using second postNewtonian wave forms*, *Phys. Rev. D* **52** (1995) 848 [gr-qc/9502040].
- [20] M. Vallisneri, *Use and abuse of the Fisher information matrix in the assessment of gravitational-wave parameter-estimation prospects*, *Phys. Rev. D* **77** (2008) 042001 [gr-qc/0703086].
- [21] A. J. K. Chua and M. Vallisneri, *Learning Bayesian posteriors with neural networks for gravitational-wave inference*, *Phys. Rev. Lett.* **124** (2020) 041102 [1909.05966].
- [22] H. Gabbard, C. Messenger, I. S. Heng, F. Tonolini and R. Murray-Smith, *Bayesian parameter estimation using conditional variational autoencoders for gravitational-wave astronomy*, [1909.06296].
- [23] S. R. Green and J. Gair, *Complete parameter inference for GW150914 using deep learning*, *Mach. Learn. Sci. Tech.* **2** (2021) 03LT01 [2008.03312].
- [24] S. R. Green, C. Simpson and J. Gair, *Gravitational-wave parameter estimation with autoregressive neural network flows*, *Phys. Rev. D* **102** (2020) 104057 [2002.07656].
- [25] L. S. Collaboration et al., *Lsc algorithm library suite*, (2020), <https://doi.org/10.7935/GT1W-FZ16>.
- [26] K. Wette, *SWIGLAL: Python and octave interfaces to the lalsuite gravitational-wave data analysis libraries*, *Accepted in SoftwareX* (2020).
- [27] B. Sathyaprakash et al., *Extreme Gravity and Fundamental Physics*, [1903.09221].
- [28] V. Kalogera et al., *Deeper, Wider, Sharper: Next-Generation Ground-Based Gravitational-Wave Observations of Binary Black Holes*, [1903.09220].
- [29] B. Sathyaprakash et al., *Multimessenger Universe with Gravitational Waves from Binaries*, [1903.09277].
- [30] B. Sathyaprakash et al., *Cosmology and the Early Universe*, [1903.09260].
- [31] L. Barack et al., *Black holes, gravitational waves and fundamental physics: a roadmap*, *Class. Quant. Grav.* **36** (2019) 143001 [1806.05195].
- [32] B. Sathyaprakash and B. Schutz, *Physics, Astrophysics and Cosmology with Gravitational Waves*, *Living Rev. Rel.* **12** (2009) 2 [0903.0338].
- [33] L. Wen and Y. Chen, *Geometrical Expression for the Angular Resolution of a Network of Gravitational-Wave Detectors*, *Phys. Rev. D* **81** (2010) 082001 [1003.2504].
- [34] W. Zhao and L. Wen, *Localization accuracy of compact binary coalescences detected by the third-generation gravitational-wave detectors and implication for cosmology*, *Phys. Rev. D* **97** (2018) 064031 [1710.05325].
- [35] C. L. Rodriguez, I. Mandel and J. R. Gair, *Verifying the no-hair property of massive compact objects with intermediate-mass-ratio inspirals in advanced gravitational-wave detectors*, *Phys. Rev. D* **85** (2012) 062002 [1112.1404].
- [36] B. S. Sathyaprakash and S. V. Dhurandhar, *Choice of filters for the detection of gravitational waves from coalescing binaries*, *Phys. Rev. D* **44** (1991) 3819.
- [37] E. Poisson, *Gravitational waves from inspiraling compact binaries: The Quadrupole moment term*, *Phys. Rev. D* **57** (1998) 5287 [gr-qc/9709032].
- [38] B. Mikoczi, M. Vasuth and L. A. Gergely, *Self-interaction spin effects in inspiralling compact binaries*, *Phys. Rev. D* **71** (2005) 124043 [astro-ph/0504538].
- [39] K. Arun, A. Buonanno, G. Faye and E. Ochsner, *Higher-order spin effects in the amplitude and phase of gravitational waveforms emitted by inspiraling compact binaries: Ready-to-use gravitational waveforms*, *Phys. Rev. D* **79** (2009) 104023 [0810.5336].
- [40] A. Buonanno, B. Iyer, E. Ochsner, Y. Pan and B. Sathyaprakash, *Comparison of post-Newtonian templates for compact binary inspiral signals in gravitational-wave detectors*, *Phys. Rev. D* **80** (2009) 084043 [0907.0700].
- [41] A. Bohé, S. Marsat and L. Blanchet, *Next-to-next-to-leading order spin-orbit effects in the gravitational wave flux and orbital phasing of compact binaries*, *Class. Quant. Grav.* **30** (2013) 135009 [1303.7412].
- [42] A. Bohé, G. Faye, S. Marsat and E. K. Porter, *Quadratic-in-spin effects in the orbital dynamics and gravitational-wave energy flux of compact binaries at the 3PN order*, *Class. Quant. Grav.* **32** (2015) 195010 [1501.01529].
- [43] C. K. Mishra, A. Kela, K. Arun and G. Faye, *Ready-to-use post-Newtonian gravitational waveforms for binary black holes with nonprecessing spins: An update*, *Phys. Rev. D* **93** (2016) 084054 [1601.05588].
- [44] ASTROPY collaboration, *Astropy: A Community Python Package for Astronomy*, *Astron. Astrophys.* **558** (2013) A33 [1307.6212].
- [45] ASTROPY collaboration, *The Astropy Project: Building an Open-science Project and Status of the v2.0 Core Package*, *Astron. J.* **156** (2018) 123 [1801.02634].
- [46] P. A. Brodtkorb and J. D'Errico, *Documentation: numdifftools*, (2019), <https://numdifftools.readthedocs.io/en/latest/index.html>.
- [47] LIGO SCIENTIFIC, VIRGO collaboration, *GW190521: A Binary Black Hole Merger with a Total Mass of 150 M_{\odot}* , *Phys. Rev. Lett.* **125** (2020) 101102 [2009.01075].
- [48] LIGO SCIENTIFIC, VIRGO collaboration, *GW190814: Gravitational Waves from the Coalescence of a 23 Solar Mass Black Hole with a 2.6 Solar Mass Compact Object*, *Astrophys. J. Lett.* **896** (2020) L44 [2006.12611].
- [49] B. D. Lackey and L. Wade, *Reconstructing the neutron-star equation of state with gravitational-wave detectors from a realistic population of inspiralling binary neutron stars*, *Phys. Rev. D* **91** (2015) 043002 [1410.8866].
- [50] L. Wade, J. D. Creighton, E. Ochsner, B. D. Lackey, B. F. Farr, T. B. Littenberg et al., *Systematic and statistical errors in a bayesian approach to the estimation of the neutron-star equation of state using advanced gravitational wave detectors*, *Phys. Rev. D* **89** (2014) 103012 [1402.5156].
- [51] LSC, *Power spectral densities (psd) release for gwtc-1*, (2019), <https://dcc.ligo.org/LIGO-P1900011/public>.
- [52] S. Husa, S. Khan, M. Hannam, M. Pürrer, F. Ohme, X. Jiménez Forteza et al., *Frequency-domain gravitational waves from nonprecessing black-hole binaries. I. New numerical waveforms and anatomy of the signal*, *Phys. Rev. D* **93** (2016) 044006 [1508.07250].
- [53] S. Khan, S. Husa, M. Hannam, F. Ohme, M. Pürrer,

- X. Jiménez Forteza et al., *Frequency-domain gravitational waves from nonprecessing black-hole binaries. II. A phenomenological model for the advanced detector era*, *Phys. Rev. D* **93** (2016) 044007 [[1508.07253](#)].
- [54] S. Borhanian, A. Dhani, A. Gupta, K. G. Arun and B. S. Sathyaprakash, *Dark Sirens to Resolve the Hubble–Lemaître Tension*, *Astrophys. J. Lett.* **905** (2020) L28 [[2007.02883](#)].
- [55] A. Gupta, S. Datta, S. Kastha, S. Borhanian, K. Arun and B. Sathyaprakash, *Multiparameter tests of general relativity using multiband gravitational-wave observations*, *Phys. Rev. Lett.* **125** (2020) 201101 [[2005.09607](#)].
- [56] K. Arun, B. R. Iyer, M. Qusailah and B. Sathyaprakash, *Probing the non-linear structure of general relativity with black hole binaries*, *Phys. Rev. D* **74** (2006) 024006 [[gr-qc/0604067](#)].
- [57] C. Messick et al., *Analysis Framework for the Prompt Discovery of Compact Binary Mergers in Gravitational-wave Data*, *Phys. Rev. D* **95** (2017) 042001 [[1604.04324](#)].
- [58] A. H. Nitz, T. Dal Canton, D. Davis and S. Reyes, *Rapid detection of gravitational waves from compact binary mergers with PyCBC Live*, *Phys. Rev. D* **98** (2018) 024050 [[1805.11174](#)].
- [59] C. J. Moore, D. Gerosa and A. Klein, *Are stellar-mass black-hole binaries too quiet for LISA?*, *Mon. Not. Roy. Astron. Soc.* **488** (2019) L94 [[1905.11998](#)].
- [60] B. J. Owen, *Search templates for gravitational waves from inspiraling binaries: Choice of template spacing*, *Phys. Rev. D* **53** (1996) 6749 [[gr-qc/9511032](#)].
- [61] B. J. Owen and B. Sathyaprakash, *Matched filtering of gravitational waves from inspiraling compact binaries: Computational cost and template placement*, *Phys. Rev. D* **60** (1999) 022002 [[gr-qc/9808076](#)].
- [62] B. F. Schutz, *Networks of gravitational wave detectors and three figures of merit*, *Class. Quant. Grav.* **28** (2011) 125023 [[1102.5421](#)].
- [63] K. Kuns, V. Srivastava, E. Hall, M. Evans and S. Ballmer (2020), <https://dcc.cosmicexplorer.org/CE-T2000007>.